JGR Atmospheres

RESEARCH ARTICLE
10.1029/2019JD030591

A Comparison of AMPS Forecasts Near the Ross Sea Polynya With Controlled Meteorological Balloon Observations

Ethan R. Dale[1,2], Marwan Katurji[3], Adrian J. McDonald[1,2], Paul Voss[4], Wolfgang Rack[2], and Daisuke Seto[3]

[1]School of Physical and Chemical Sciences, University of Canterbury, Christchurch, New Zealand, [2]Gateway Antarctica, University of Canterbury, Christchurch, New Zealand, [3]Center for Atmospheric Research, University of Canterbury, Christchurch, New Zealand, [4]Smith College, Picker Engineering Program, Northampton, MA, USA

Abstract This study presents atmospheric boundary layer observations made over the Ross Sea using a long-duration Controlled Meteorological (CMET) balloon and a comparison with Antarctic Mesoscale prediction System (AMPS) forecasts. The CMET balloon was launched on 22 November 2017 at 1230 UTC; this flight performed 31 repeated soundings of the atmospheric boundary layer over a period of 70 hr. During the flight the balloon made close passes of the open Terra Nova Bay and Ross Sea polynyas. We use the AMPS forecast during the flight to understand the influence of the polynya on the air sampled by the CMET balloon. Balloon observations of temperature, humidity, and wind velocity generally agree with AMPS forecasts, with the largest disparities in the wind direction field during periods of light wind and when the path of the balloon was near complex topography. To understand the thermodynamic interaction between these polynyas and the atmospheric volume sampled by the balloon, a Lagrangian trajectory model forced by AMPS winds was used to calculate the total and partial derivatives of potential temperature as well as the total water mixing ratio. This allowed us to assess the thermodynamic profile of the overlying atmospheric boundary layer. Based on analysis of the AMPS forecast, we were able to identify a region of warming air with an area of 20,000 km^2, centered over the Ross Sea Polynya which was providing a strong heat source at the time of the balloon flight.

Key Points:
- Controlled Meteorological balloon observations over the Ross Sea are compared to Antarctic Mesoscale Prediction System forecasts
- We examine the influence of the Ross Sea Polynya on the atmosphere using a Lagrangian trajectory model forced by forecast winds
- The Ross Sea Polynya is identified as a significant source of heat within forecast output using Lagrangian and Eulerian derivatives

Correspondence to:
E. R. Dale,
ethan.dale@pg.canterbury.ac.nz

Citation:
Dale, E. R., Katurji, M., McDonald, A. J., Voss, P., Rack, W., & Seto, D. (2020). A comparison of AMPS forecasts near the Ross Sea polynya with Controlled Meteorological balloon observations. *Journal of Geophysical Research: Atmospheres*, *125*, e2019JD030591. https://doi.org/10.1029/2019JD030591

Received 5 MAR 2019
Accepted 10 SEP 2020
Accepted article online 13 SEP 2020

1. Introduction

Meteorological variability over the Ross Sea and Ross Ice Shelf (RIS) is strongly impacted by synoptic and mesoscale dynamics driven by orographic features such as the Trans-Antarctic Mountains, surrounding ice sheets, and the mixed surface cover (open waters and sea ice) of the Ross Sea (Costanza et al., 2016; Cassano et al., 2016; Nigro et al., 2012). These features induce both synoptic and mesoscale modulations in the lower atmosphere, resulting in the observed, highly variable temperature and precipitation patterns. Radiatively cooled air over the East and West Antarctic Ice Sheets feed katabatic flows down steep glacier valleys from East Antarctica, and more moderate slopes from West Antarctica, onto the RIS (Bromwich, 1989). These katabatic flows frequently combine with synoptic-scale cyclones over the Southern Ross Sea, which produce pressure gradients parallel to the Trans-Antarctic Mountains, driving a strong, southerly airflow along the barrier formed by the Trans-Antarctic Mountains (Parish & Bromwich, 1997, 1998). This climatological airflow pattern is known as the Ross Air Stream (RAS) (Coggins et al., 2014; Costanza et al., 2016; Parish et al., 2006).

The strong winds during RAS events are known to cause the breakup of sea ice in the polynya region and the advection of sea ice from the Ross Sea Polynya (RSP), a large coastal polynya that forms in the Southern Ross Sea (Bromwich et al., 1998; Dale et al., 2017). The combination of thin ice and exposed warm water relative to the overlying atmosphere within the RSP is responsible for large ocean-to-atmosphere fluxes of heat and moisture (Batrak & Müller, 2018). Previous work detailed in Bourassa et al. (2013) has identified that the representation of sea ice in weather prediction models has important consequences for the atmosphere-sea ice interaction on a wide range of spatiotemporal scales, since sea ice is a dominant constraint for atmospheric surface fluxes in polar regions. This in turn results in accelerated sea ice production rates (Tamura et al., 2008).

Sea Ice cover is the most dynamic component of the Antarctic cryosphere, and any change is related to variations in the atmosphere and oceanic patterns over a multitude of scales (Bourassa et al., 2013). The observed increase of Antarctic sea ice extent over the satellite observation period is largely driven by changes in the western Ross Sea and likely related to feedbacks in the ice-ocean-atmosphere system (Holland & Kwok, 2012). Potentially also influenced by the Amundsen Sea Low which also has a known influence on the weather patterns in the region (Coggins & McDonald, 2015). The highest sea ice production rates are observed within coastal polynyas, which control the production of high-salinity shelf water and thermohaline circulation (Drucker et al., 2011). Despite this climatological significance and the possible link between increased sea ice production and meteorological variability, the boundary layer processes linking the synoptic scale and mesoscale are still relatively underexplored in this area. This is largely due to the lack of suitable measurement technologies and logistic limitations associated with this hostile region.

The Antarctic coast's complex topography and the effect of variable sea ice cover can introduce significant departures from large-scale influences with localized impacts. For example, it is well established that prominent coastal topographies, like the Antarctic Peninsula, interact with synoptic or large cyclonic weather systems to shed smaller cyclonic eddies downstream of the topography and develop strong downslope storms that have implications on the surface heat budget and snow mass balance (Elvidge et al., 2015). The high frequency of occurrence of mesocyclones in the Terra Nova Bay region is of particular interest. These occur as a result of the convergence of the offshore surface wind field with northerly warm air currents and sea ice variability in this area (Carrasco & Bromwich, 1993). Heinemann (1990) studied a 6-year climatology of mesocyclones in the Weddell Sea and concluded that the majority of the mesocyclones occurred over ice-free areas and areas of converging offshore winds from valley tributaries. These studies reinforce the importance of the feedback mechanisms of the surface on such weather systems. These are usually maximized as cold air currents of a continental origin interact with the relatively warmer open water within polynyas, causing an uptake of moisture and heat and a resultant destabilization into mesocyclonic systems. Several other studies (Bromwich, 1991; Carrasco & Bromwich, 1993; Turner & Thomas, 1994) have suggested that localized weather systems occur during the open water seasons, driven by the main driving mechanism of heat and moisture uptake by the atmosphere. These results exemplify the dynamic nature of the atmosphere-sea ice-ocean interactions within the Ross Sea region.

In the context of regional climate predictions and both surface temperature and precipitation variability, it has become more important to assess the skill of our dynamical down-scaling models in representing these weather patterns in the Antarctic. Pezzi et al. (2016), when down-scaling climate model outputs, showed a 46% increase in mesocyclone frequency when compared to the lower-resolution ERA-Interim reanalyses. This result was mainly attributed to the enhanced resolution and better resolved boundary layer dynamics due to their smaller spatial scales. Pezzi et al. (2016) also attributes an increase in mesocyclone frequency to areas of large anomalies in surface sensible heat flux such as the edge of the sea ice, during cold air outbreaks over warmer lower-latitude sea surface temperatures, and over polynyas (Bracegirdle & Kolstad, 2010; Papritz & Pfahl, 2016; Papritz et al., 2015). Petrelli et al. (2008) demonstrated the importance of high-resolution models for sea ice modeling. In a coupled sea ice-atmosphere model, winter sea ice formation within the Ross Sea and Terra Nova polynyas was found to double when model resolution was increased by a factor of 5.

Flight and ground operations in Antarctica rely upon weather forecasts, such as the Antarctic Mesoscale Prediction System (AMPS). Several studies have sought to validate this model using surface-based automatic weather stations, including Nigro et al. (2011, 2012), Bromwich et al. (2013), and Jolly et al. (2016). These studies have found that the greatest errors in AMPS simulations occur in regions of complex topography and low wind speeds. The accuracy of this model is limited by its spatial grid resolution in regions such as the Antarctic coast, where complex topography exists (Bromwich et al., 2005).

The main objective of this study is to compare observations made using Controlled Meteorological (CMET) balloons with predictions made by the AMPS forecasts. These observations were initiated from the complex coastal topographies of the western side of the Ross Sea region. Balloons then drifted with the synoptic, regional, and local weather systems over the variable surface cover of the Ross Sea including the Terra Nova Bay and Ross Sea polynyas. CMET balloons are designed for flights within the lower troposphere with height-controlled flights capable of repeated vertical probing of the atmospheric boundary layer over several days. These balloons have a payload mass similar to that of a standard weather balloon (Voss et al., 2012),

and their unique design allows observations of inaccessible regions, such as the Ross Sea which contains complex coastal topography as well as vast areas of open water and sea ice.

CMET balloons have previously been successfully tested in both the Arctic and Antarctic regions. Voss et al. (2012) report a series of CMET launches from Svalbard during 2010 and 2011; the longest of these lasted for 24 hr and completed 18 vertical profiles. Roberts et al. (2016) compare data collected from five of these launches in Svalbard with model hindcasts made by ERA-Interim and the Arctic System Reanalysis (ASR). They found that the higher-resolution ASR modeled the observations made by the CMET balloons more accurately than ERA-Interim. A CMET balloon was also launched from Troll Station, Antarctica, by Stenmark et al. (2014) in January 2012. Hole et al. (2016) also launched two CMET balloons from Aboa Station, Antarctica, in January 2013. These had flight times of 60 and 106 hr, respectively, and the latter observed a mesoscale anticyclone over the Weddell Sea.

Here we use data from one of four CMET flights launched in 2017 from Mario Zucchelli station, located in Terra Nova Bay Antarctica (Figure 2) (74.695°S, 164.096°E). Two of these flights produced relevant data over the Ross Sea, spanning 18 and 70 hr of flight time. The other two balloons were less successful; the first was overpressurized during inflation and suffered a loss of control 8 hr into the flight. The flight was terminated safely, and the balloon therefore provided data of limited use. The final balloon suffered an electrical fault immediately after launch that prevented communications with the balloon; thus, no data were able to be collected from this balloon.

In this study we focus our analysis on data retrieved from the CMET balloon that provided the longest period of continuous observations. These CMET observations are compared to predictions made by AMPS, with particular focus on a 24 hr period starting at 0800 UTC on 23 November 2017, in which the balloon flew into a region of air that was impacted by heat and moisture fluxes from the RSP.

Another objective of this work is to quantify the thermodynamic representation of the Terra Nova Bay and Ross Sea polynyas using AMPS and CMET observations. This is achieved by the calculation of Lagrangian and Eulerian derivatives of total water mixing ratio (TWMR) and potential temperature predicted by AMPS. The unique height-controlled balloon observations of the Ross Sea region's atmospheric boundary layer, combined with moisture and heat budgeting from a numerical mesoscale model, allow new insights into AMPS skill in resolving surface-atmospheric exchange processes. Finally, we demonstrate a successful observational method for future regional weather and climate studies in this region.

2. Data and Methods

2.1. CMET Balloons

CMET Balloons are altitude-controlled helium balloons designed to make flights with durations up to several days at altitudes less than 4 km (Voss et al., 2012). During flight CMET balloons measure air temperature, pressure, relative humidity (RH), and GPS location. From the GPS location, the balloon's velocity can be derived, and thus the local wind can be inferred. Data are transmitted back in near-real time through the usage of an onboard Iridium 9603 satellite modem. This satellite connection is also used to receive commands, controlling the balloon's altitude and data acquisition frequency during flight.

Each balloon consists of two bladders: a high-pressure reservoir and an outer buoyancy bladder that is kept at atmospheric pressure. By pumping helium between the two bladders, the buoyancy of the balloon can be altered, allowing control over the balloon's altitude. This gives the CMET balloon a unique capability to make repeated soundings through the same altitude range. A schematic of the CMET balloon is shown in Figure 1.

The CMET balloon's 230 g payload comprises the control electronics, GPS receiver, satellite modem, pump valve system, lithium polymer battery, photovoltaic panel, aspirated T-RH sensor, and a vacuum-insulated pouch. With this insulation, the payload temperature is maintained within acceptable operating limits (typically +20 K above ambient) even at altitudes of several kilometers in the polar regions. Pressure is measured using an aviation-grade pressure sensor (Freescale MPXH6115A) with a 16-bit analog-to-digital converter (Analog Devices AD7795). During flight, altitude is determined every 10 s by interpolating pressure to the U.S. Standard Atmosphere. In postflight processing, the pressure altitude is corrected for pressure offsets using the in-flight GPS altitude (Inventek ISM420). GPS latitude and longitude provide the position during flight and are also further analyzed postflight to determine eastward (U) and northward (V) wind

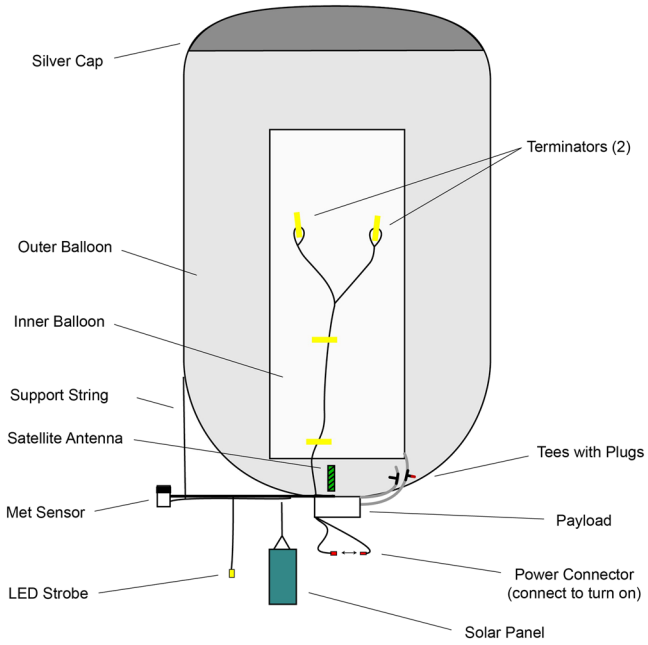

Figure 1. Schematic diagram of a CMET balloon.

speeds. The specified GPS position accuracy is ±10 m root-mean-square (RMS). Temperature is measured using a thermistor (General Electric MC65F103A) in a 10 k-Ohm divider circuit coupled to the aforementioned analog-to-digital converter. The specified thermistor accuracy is ±0.1°K over the temperature range 0 to 70°C. We note that during the flights presented here temperatures were outside this range, so the accuracy of this thermistor was likely worse than ±0.1°K. A capacitance humidity sensor (G-TUCN.34 from UPSI, covering 2% to 98% RH range over −40 to +85° C) generates a variable-frequency signal which is a function of the ambient RH with respect to water. While the humidity sensors have a specified accuracy of ±2% RH, a preflight intercomparison of the sensors indicated that the actual accuracy was substantially lower (on the order of ±10% RH).

The CMET balloon's 230 g payload comprises the control electronics, GPS receiver, satellite modem, pump valve system, lithium polymer battery, photovoltaic panel, aspirated T-RH sensor, and a vacuum-insulated pouch. With this insulation, the payload temperature is maintained within acceptable operating limits (typically +20 K above ambient) even at altitudes of several kilometers in the polar regions. Pressure is measured using an aviation-grade pressure sensor (Freescale MPXH6115A) with a 16-bit analog-to-digital converter (Analog Devices AD7795). During flight, altitude is determined every 10 s by interpolating pressure to the U.S. Standard Atmosphere. In postflight processing, the pressure altitude is corrected for pressure offsets using the in-flight GPS altitude (Inventek ISM420). GPS latitude and longitude provide the position during flight and are also further analyzed postflight to determine eastward (U) and northward (V) wind speeds. The specified GPS position accuracy is ±10 m root-mean-square (RMS). Temperature is measured using a thermistor (General Electric MC65F103A) in a 10 k-Ohm divider circuit coupled to the aforementioned analog-to-digital converter. The specified thermistor accuracy is ±0.1°K over the temperature range 0 to 70°C. We note that during the flights presented here temperatures were outside this range, so the accuracy of this thermistor was likely worse than ±0.1°K. A capacitance humidity sensor (G-TUCN.34 from UPSI, covering 2% to 98% RH range over −40 to +85° C) generates a variable-frequency signal which is a function of the ambient RH with respect to water. While the humidity sensors have a specified accuracy of ±2% RH, a preflight intercomparison of the sensors indicated that the actual accuracy was substantially lower (on the order of ±10% RH).

As the altitude that the balloon flies at is changed, it often passes through a vertical wind shear. This can be used to provide limited control over the balloon's flight path, providing added flexibility during flights. Although the balloon is equipped with a solar panel, power management remains a major challenge

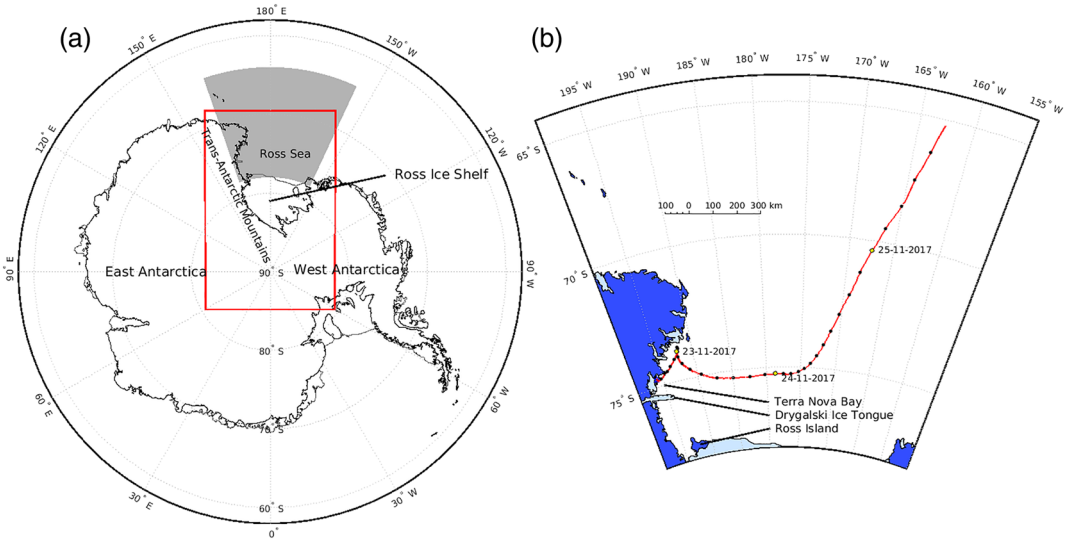

Figure 2. (a) Map of Antarctica, showing relevant geographical features. The red box represents the spatial extent of the AMPS Domain 3 grid. The gray region indicates the area shown in panel (b). (b) Map of Ross Sea region showing the CMET flight path in red. The yellow dots represent the position of the balloon at 0000 UTC on the dates indicated, while the black dots are spaced at 2 hr intervals.

throughout a flight. During periods of limited solar availability, the rate that data is sampled can be decreased to minimize power draw. This results in the data having a variable temporal resolution.

Hysteresis was observed between ascending and descending profiles of temperature and RH measured by the CMET balloon. This is likely due to radiative heating of the slowly ascending balloon. Effectively a heated pocket of air enveloping the balloon is formed, which then rises alongside the balloon as it ascends. On descending profiles, this effect would be reduced as the heated air would continue to rise buoyantly away from the sinking balloon. Sensors were mounted on an 800 mm boom to increase the distance between them and the balloon with the aim of minimizing this effect. Unfortunately, hysteresis was still observed. Consequently, measurements of temperature and RH made during ascending profiles are excluded from our analysis. Measurements of wind speed and direction, derived from the GPS location of the balloon, were not subject to this procedure.

RH measurements were calibrated postflight to agree with the measurements made by radiosonde balloons regularly launched from Mario Zucchelli station. Vaisala RS92-SGP radiosondes were launched twice daily, less than 1 km from the CMET launch site. CMET balloons were launched 1–1.5 hr after a radiosonde launch as radiosonde data were used to determine appropriate launch conditions for the CMET balloon. The first descending pass of each CMET flight was compared to the radiosonde observations. Radiative heating on the radiosonde balloons does not have a significant influence as the balloon rises much more rapidly than the CMET balloon, allowing the ascending profile from the radiosonde to be used. A simple constant was added to the CMET RH observations, so that a least squares difference between the first descending pass of the CMET balloon and the ascent profile of the radiosonde was achieved.

The CMET balloon was launched at 1230 UTC on 22 November 2017 from Mario Zucchelli station (74.695°S, 164.096°E). This balloon initially traveled northeast, roughly parallel to the Antarctic coast, for a period of 14 hr. The balloon then continued eastward toward the center of the Ross Sea, passing just north of the RSP by 2000 UTC on 23 November. After 0600 UTC on 24 November, the synoptic-scale flow changed direction, resulting in the balloon being carried northeast out of the Ross Sea toward a large cyclone in the Southern Ocean (Figure 2). The total flight time of the balloon was just over 70 hr, though we focus on just over the central 30 hr of this period. For the majority of the first half of this flight, until 2000 UTC on 23 November, the balloon performed repeated soundings between 50 and 600 m altitude (Figure 2). Unfortunately, solar charging was limited due to overcast conditions, and after 2000 UTC on 23 November a decision was made to stop the balloon soundings; the balloon remained at an altitude close to 500 m after this point, and the data rate was decreased in order to conserve the balloon's battery power.

2.2. AMPS

The AMPS is a version of the Weather Research and Forecasting (WRF) model modified for polar regions (Powers et al., 2012). AMPS operates over several domains that cover a range of horizontal spatial extents and grid resolutions. This study analyzes output from AMPS Domain 3, which operates on a 2.67 km horizontal spatial resolution and has an output frequency of 1 hr. In this study we use AMPS WRF version 24 documented online (at https://www2.mmm.ucar.edu/rt/amps/information/amps_esg_data_info.html).

Domain 3 covers a $1,802 \times 2,766$ km area spanning the Ross Sea, the RIS, and the South Pole and is shown as a red rectangle in Figure 2a. Each AMPS domain uses 61 vertical levels, with 60 additional half levels between each full level. The model top is at 10 hPa, and within the top 7.5 km vertical velocity dampening is applied. AMPS forecasts are issued at midday and midnight UTC. Forecasts output by the higher-resolution Domains 3, 5, and 6 have a output frequency of 1 hr spanning 40 hr, resulting in considerable overlap between consecutive forecasts. Forecasts for the lower-resolution Domains 1 and 2 instead cover 121 hr with a 3 hr output frequency.

AMPS obtains initial and boundary conditions from NCEP 0.25° GFS model output which operates on a 6 hr time resolution. Sea surface temperature data are obtained from the daily NCEP 0.5° model. Near-real-time ice and snow extent (NISE) data provide input sea ice concentration (SIC) values (Brodzik & Stewart, 2016). Data are assimilated using WRFVAR 3-D variational data assimilation, with sea ice fields being updated in every other forecast.

The polar WRF model used in AMPS utilizes a specific set of physics options. Cloud microphysics are modeled using the WRF single-moment five-class scheme which includes mixed phase processes and supercooled water. The rapid radiative transfer model for GCMs models longwave radiation, while shortwave radiation is modeled by the Goddard shortwave scheme. The Monin-Obukhov (Janjic Eta) scheme models the surface layer, and surface physics are modeled using the Noah land surface model. The boundary layer is modeled using the Mellor-Yamada-Janjic (Eta) scheme. The higher-resolution domains, including Domain 3, do not include a cumulus parameterization scheme. Sea ice is implemented using a fractional method; in order to determine surface fluxes, the surface layer scheme is called twice, once for the area of open water and a second time for the area of sea ice within the cell. The resulting fluxes are then area averaged based on grid cell SIC to determine the total flux within the cell.

2.3. Lagrangian Trajectories

Lagrangian trajectories were used to trace the pathway of hypothetical air parcels. These were calculated using the AMPS forecast wind vectors (Powers et al., 2012), following the methodology detailed in Alexander et al. (2013) and Friedrich et al. (2017). Trajectories were launched from 500 m above the local surface topography and were free to move vertically as they propagated. These trajectories were started at this altitude so that they started at close to the level that the CMET balloon traveled. At each trajectory time step, a three-dimensional wind vector was interpolated within the four-dimensional (latitude, longitude, pressure, and time) AMPS fields using cubic splines. A fourth-order Runge-Kutta method was then used to propagate the trajectory path to the next time step. Trajectory calculations were performed in a local three-dimensional Cartesian grid and then converted back to a latitude, longitude, and pressure coordinate system. For each trajectory, the potential temperature and specific humidity at each time step were also calculated using a cubic spline interpolation from the AMPS grid.

A 5 min temporal resolution was used for trajectory calculations; this is considerably shorter than the 60 min output frequency of the AMPS output. The accuracy of trajectories is likely limited by the AMPS temporal resolution; therefore, using higher temporal resolution for trajectory propagation will provide diminishing returns.

From each launch site, trajectories were propagated 12 hr forward and backward from the central start time, revealing both the origin and destination of each air parcel relative to its initial location. To avoid discontinuities between consecutive forecasts, each forward/backward trajectory set was calculated entirely using data from a single, continuous issue of the AMPS forecast. Each AMPS Domain 3 forecast spans 0–39 hr and is calculated from one set of initial conditions. This results in the first 8 hr of the AMPS forecast not being used, removing potential errors due to model spin-up in AMPS (Bromwich et al., 2005; Guo et al., 2003; Jolly et al., 2016).

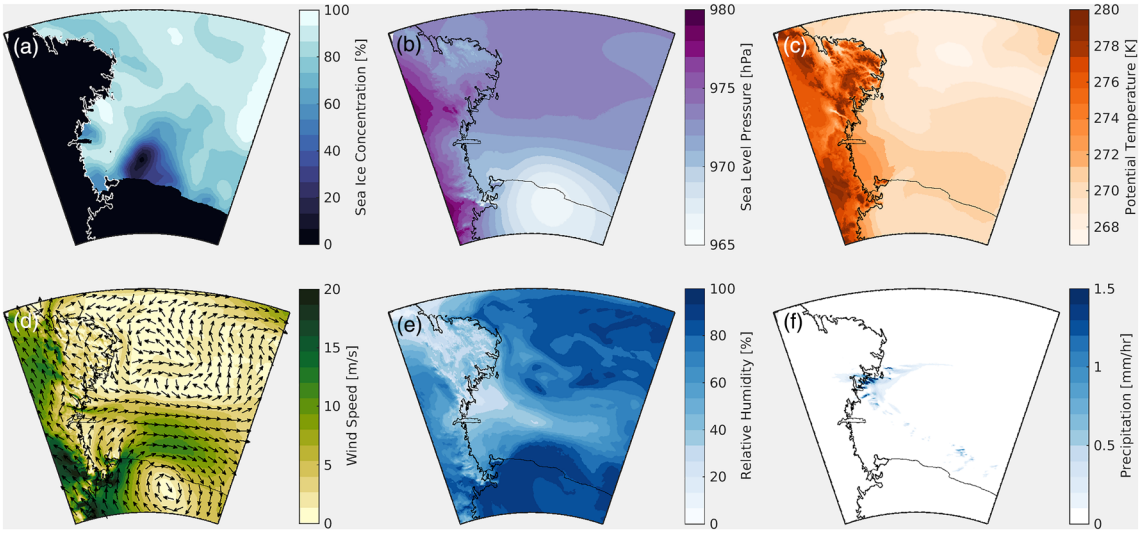

Figure 3. (a) AMPS sea ice concentration (SIC) over the Ross Sea on 23 November (b), mean sea level pressure on 23 November (c–e) Mean potential temperature, mean wind velocity, and mean relative humidity at a height of 500 m averaged over a 24 hr period starting at 0800 UTC on 23 November. (f) Mean precipitation over the same 24 hr period. As predicted by AMPS forecast issued at 0000 UTC on 23 November.

2.4. Lagrangian Spatial Average Trajectory Derivatives

Gridded Lagrangian derivatives calculated from spatial averages taken along trajectories, referred to as Lagrangian spatial average trajectory (SAT) derivatives from this point on, were derived from potential temperature and TWMR predicted by AMPS and were calculated by launching Lagrangian trajectories both forward and backward in time from each grid point. Lagrangian SAT derivatives describe the rate of change that a freely moving parcel of air would experience over the entire trajectory period but also represent a spatially averaged derivative. They therefore do not directly connect to the instantaneous Lagrangian derivatives required to calculate advection but provide a measure of how the properties of a particular air parcel change along its trajectory and therefore represent a spatial average which mimics the observations of the CMET balloons. Trajectories were launched on a 3.7 km by 3.7 km grid covering the southwestern Ross Sea. The mean derivative for a particular AMPS field was then approximated as the difference of that field at the time and location of endpoints from both the forward and backward trajectories. For this work, a trajectory length of 12 hr was used for both the forward and backward component, resulting in a mean derivative of a 24 hr period. Lagrangian derivatives were calculated using a two-dimensional grid of launch sites covering the western Ross Sea, with constant initialization heights of 250, 500, and 1,000 m above the ground surface. Trajectories were allowed to freely propagate in three spatial dimensions.

3. Results

Figure 3 displays atmospheric parameters and sea ice conditions associated with 23 November, to provide context for later discussion. The AMPS SIC on 23 November (Figure 3a) indicates that the RSP was open during this period, with 0% SIC being measured at the center of the polynya. Decreased SICs were also found in the McMurdo and Terra Nova Bay polynyas, although the SIC within these regions do not fall below 40%.

Average mean sea level pressure predicted by the AMPS forecast issued at 0000 UTC on 23 November averaged over a 24 hr period, starting at 0800 UTC on 23 November, is plotted in Figure 3b. Figures 3c–3e show potential temperature, wind speed and direction, and RH averaged over the same 24 hr period at 500 m above ground level. A cyclone is present over the northern edge of the RIS, driving strong, southerly winds connected to a RIS air stream event over the RSP. A weaker anticyclonic system lies over the northwestern Ross Sea, enhancing the offshore flow near Terra Nova Bay also driven by the cyclone over the RIS resulting in strong, dry, westerly winds over the Southern Ross Sea.

The RH field (Figures 3e) shows two regions of very humid air over the RIS and Northern Ross Sea. These regions are separated by a relatively dry band of air. This band of dry air originates over Terra Nova Bay, with cool, dry air flowing down from Victoria Land and being drawn east by both the cyclone to the south and

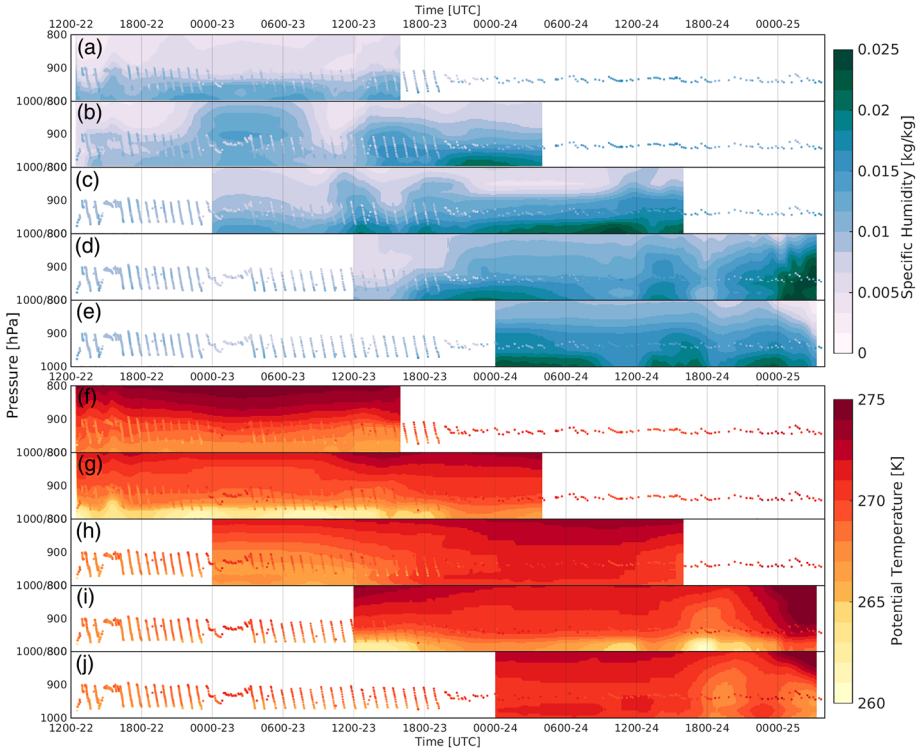

Figure 4. (a–e) Specific humidity forecast by AMPS on a pressure-time plane following the CMET flight path. The individual panels represent consecutive AMPS forecasts. The overlying dots represent colocated CMET observations. (f–j) As for a–e but instead showing potential temperature.

the anticyclone to the north. Meanwhile, the anticyclone to the north draws moist air that was previously north of the ice edge eastward. Figure 3f shows the mean precipitation rate over a 24 hr period, starting at 0800 UTC on 23 November. This shows a small area of precipitation over the Antarctic coast, just north of Terra Nova Bay, trapped between the cyclone and the anticyclone.

Figure 4 and Table 1 provide a comparison of specific humidity and temperature predicted by AMPS at five different forecast initializations (from 0000 UTC on 22 November to 0000 UTC on 24 November at 12 hr intervals) with that observed by the CMET balloon along its flight path. Similarly, Figure 5 and Table 1 compare wind strength and direction forecast by AMPS for the same five forecast initializations with CMET observations.

A vertical surface which follows the flight path of the CMET balloon in space and time was derived, producing a two-dimensional curtain along the flight path of the balloon. AMPS variables were interpolated using cubic splines from the four-dimensional (latitude, longitude, pressure, and time) AMPS grid to this

Table 1
The Mean Values Over the Forecast Period for the Potential Temperature, Specific Humidity, and Wind Speed Are Shown for AMPS Output and the CMET Observations for a Range of Forecast Start Dates and Times

Forecast time-date	Potential temperature (K)			Specific humidity (kg/kg)			Wind speed (m/s)		
(November)	CMET	AMPS	RMSE	CMET	AMPS	RMSE	CMET	AMPS	RMSE
0000-22	268.87	268.95	1.23	0.0088	0.0089	0.0021	5.81	3.74	11.01
1200-22	269.25	268.26	1.57	0.0090	0.0114	0.0037	6.25	3.41	9.61
0000-23	269.56	269.43	3.40	0.0103	0.0132	0.0040	6.76	5.18	8.96
1200-23	270.12	269.73	3.18	0.0112	0.0142	0.0052	8.92	4.38	6.00
0000-24	270.48	269.90	4.05	0.0123	0.0163	0.0053	10.66	2.63	7.36

Note. The root-mean-square errors (RMSE) between the AMPS output and the CMET observations are also displayed.

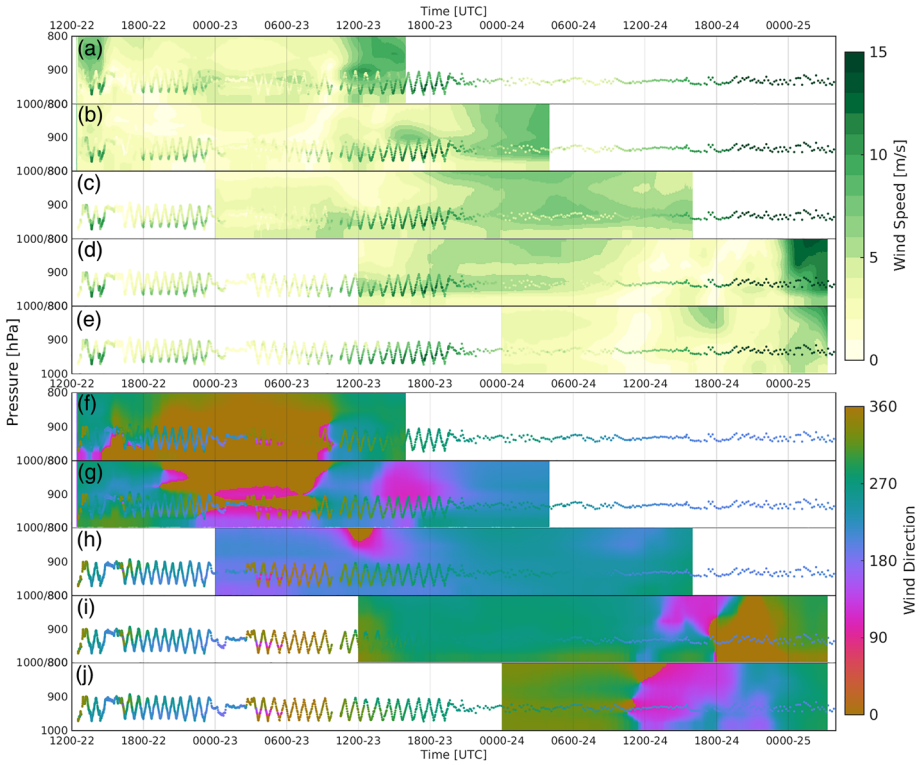

Figure 5. (a–e) Wind speed interpolated from the forecast by AMPS onto a pressure-time plane following the CMET flight path. The individual panels represent consecutive AMPS forecasts. The overlying dots represent colocated CMET observations. (f–j) As for a–e but instead showing wind direction.

two-dimensional (pressure and time) surface. CMET observations were then plotted over these surfaces using the same color scheme, allowing for a qualitative comparison of AMPS and CMET observations.

Table 1 displays the mean values for AMPS model output and CMET observations for potential temperature, specific humidity, and wind speed for a range of forecast issue times and dates. Table 1 also displays the root-mean-square error (RMSE) between colocated and synchronous AMPS model output and CMET observations for potential temperature, specific humidity, and wind speed averaged over the forecast period. Examination of Table 1 shows that the difference between the mean values from AMPS output and CMET observations is a minimum for the AMPS forecast issued at 0000 UTC on 23 November for wind speed. During this period, the bias for potential temperature was also very low, with the bias at 0000 UTC on 22 November being slightly smaller. This is not true for the specific humidity field, but as detailed in section 2.1 the absolute values of the RH measurements made by the CMET balloon are quite uncertain, so we choose to ignore this fact. Given that this AMPS forecast displays a small bias in the potential temperature and wind speed and also represents the period where the CMET balloon is closest to the RSP, we focus on this forecast in the rest of this study. However, we note that the RMSE increases from the first to last forecast period in both potential temperature and specific humidity. Thus, there is clearly evidence of misrepresentation of some features of the atmospheric state in the AMPS forecast which must be borne in mind when interpreting future results, though we also note that this may partially reflect the fact that CMET stops vertical profiling in the latter portion of these periods which will impact the RMSE.

Examination of the differences between the CMET observations and the corresponding AMPS model output as a function of time also shows a significant variation across the various forecasts (see Figures 4 and 5). However, this is largely dominated by the change between the period where the balloon was profiling and after that period. This suggests that the biases between the CMET observations and the AMPS forecasts and the RMSE were strongly altitude dependent. In particular, we note that the potential temperatures had larger errors near the surface, as did the wind speeds. This may partially explain issues highlighted later on around disparities associated with sensible and latent heat fluxes.

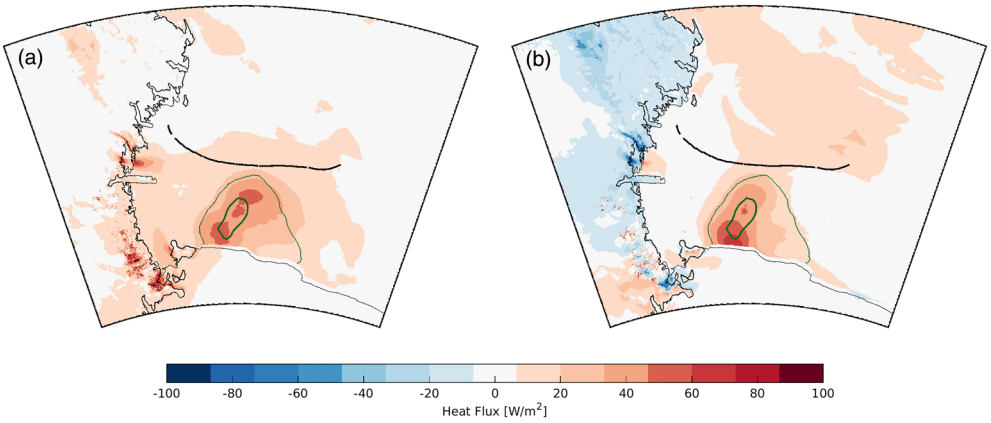

Figure 6. (a) Mean latent heat flux on 23 November from AMPS forecast issued at 0000 UTC on 23 November. (b) Mean sensible heat flux over the same time period. The black lines indicate the CMET flight path during this period. The thick and thin green lines indicate the 15% and 50% SIC isopleths, respectively.

Inspection of the AMPS predictions in Figure 4 reveals large variations between consecutive forecasts at the same time. For example, between 0000 UTC and 0600 UTC on 23 November, a zone of high specific humidity was predicted above 900 hPa by the forecast issued at 1200 UTC on 22 November. This moist area was not predicted by the forecasts issued at 0000 UTC on 22 and 23 November. Similarly, the forecast issued at 1200 UTC on 22 November predicted a low-level temperature inversion between 2000 UTC on 22 November and 1500 UTC on 23 November. This feature was not predicted by the forecasts immediately preceding and following.

AMPS performed comparatively more poorly when predicting wind speed and direction. Wind speed over the period from 1800 UTC on 22 November to 0000 UTC on 23 November proved particularly difficult for AMPS to model with CMET tending to provide higher wind speeds than AMPS, especially near the surface. From around 0800 UTC on 23 November CMET also observed higher wind speeds than the AMPS forecast, though between 0000 UTC and 0800 UTC on 23 November the AMPS forecast is very close to the values measured by CMET. During this time, the southerly winds observed by the CMET balloon weakened and gave way to strengthening northerly winds. Following the wind shift at 0300 UTC on 23 November, the CMET balloon, which was close to the Antarctic coast, observed winds from a variable direction that were not accurately modeled by any of the AMPS forecasts. Within regions of varied topography, the quality of AMPS forecasts is known to be limited by the grid resolution, which likely explains this issue (Bromwich et al., 2005; Jolly et al., 2016). During the period examined in this paper, 0800 UTC on 23 November to 0800 UTC on 24 November, the differences between the AMPS output and the CMET observations were close to the minimum observed (see Table 1).

Figure 6 shows the mean latent and sensible heat fluxes over a 24 hr period, starting at 0800 UTC on 23 November, predicted by the AMPS forecast issued at 0000 UTC on 23 November (Figures 4c and 4h). The thick and thin green contours in Figure 6 represent 15% and 50% SIC, respectively, and indicate the position and size of the RSP during this period. The strongest upward latent and sensible heat fluxes are predicted within both the Ross Sea and Terra Nova Bay polynyas. This indicates that AMPS modeled heat fluxes from the warm, open ocean into the atmosphere, and evaporation of sea water and consequent moisture fluxes. Sea water has a freezing point of approximately −1.8°C; therefore, open water provides a large source of heat to the cooler air above, the air temperature at the nearby Laurie II weather station being −8°C. These latent and sensible heat fluxes were of moderate magnitude compared to values derived over polynya (Bourassa et al., 2013; Fiedler, 2010). We note that the comparison of the low-level wind speeds between the CMET observations and the AMPS output suggests that the AMPS low-level wind speeds are overestimates of the reality, given that the temperatures are rather similar; this means that the sensible and latent heat fluxes estimated by AMPS are likely underestimates.

Figures 7a and 7b show the Lagrangian SAT and Eulerian derivatives for the TWMR predicted by AMPS over a 24 hr period, starting at 0800 UTC on 23 November, on a surface 500 m above the ground. These derivatives are therefore centered upon 2000 UTC on 23 November. The 500 m level was selected as it relates

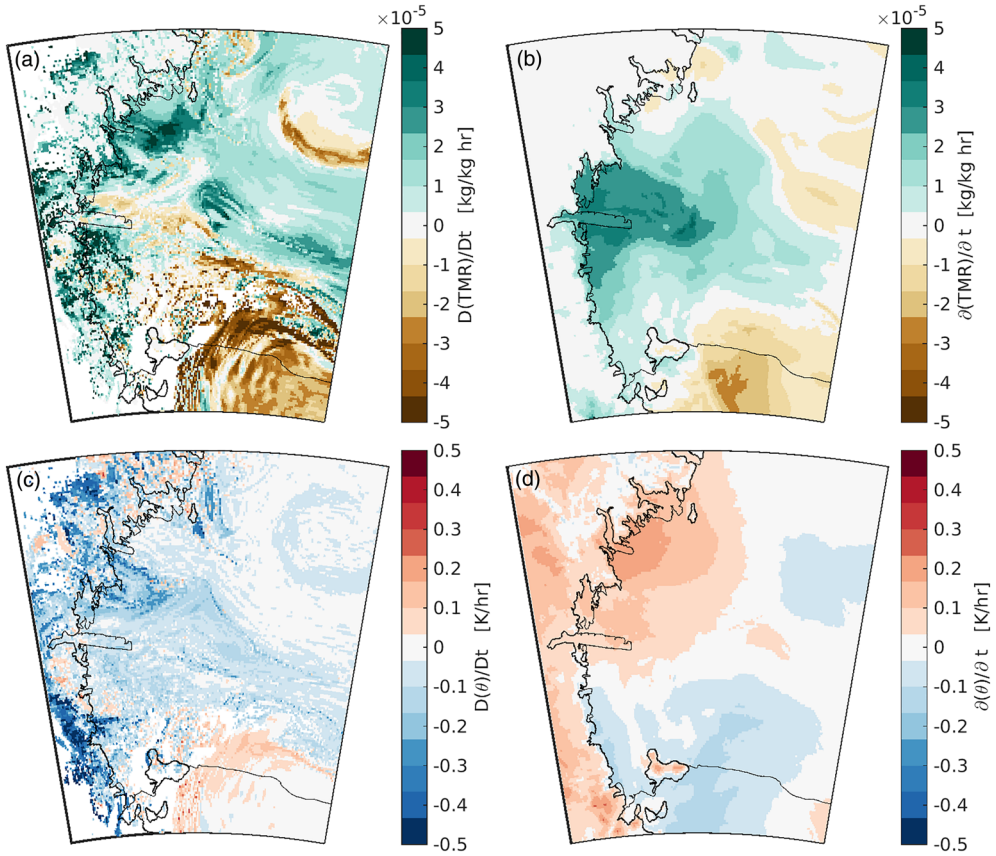

Figure 7. (a) Lagrangian SAT derivative of the total mixing ratio over a 24 hr period starting at 0800 UTC on 23 November, calculated using trajectories launched 500 m above the surface. (b) Eulerian derivative of the total water mixing ratio at 500 m over the same 24 hr period. (c) Lagrangian SAT derivative of potential temperature over the same period. (d) Eulerian derivative of potential temperature at 500 m over the same 24 hr period.

to the altitude that the CMET balloon travels after it stopped vertical profiling because of low battery power. The Lagrangian average trajectory derivative, calculated as the difference over time in the given variable between the ends of the forward and backward trajectories, represents the average rate of change that would be experienced by a free parcel of air. The Eulerian derivative, calculated as the difference in the given variable over the same period of time at a fixed location, represents the rate of change that a stationary observer would observe. We note that the trajectories used to derive the Lagrangian SAT derivative were calculated within the AMPS Domain 3 field; however, some trajectories traveled beyond the spatial bounds of this domain and were therefore not able to be continued. This causes some regions of the Lagrangian SAT derivative field to be undefined (Figure 7a). These are mostly over the Trans-Antarctic Mountains, where back trajectories follow fast-moving, directionally consistent streamlines toward the edge of the field, allowing air parcels to cover a large distance in a short time.

TWMR is defined as the sum of the mixing ratios for water vapor, cloud water, cloud ice, rain, and snow. These mixing ratios are all defined within AMPS. The Lagrangian SAT derivative of the TWMR (Figure 7a) shows that air passing over the Southern Ross Sea and over the RIS became drier during its journey, while air passing over more northern parts of the Ross Sea and the Trans-Antarctic Mountains became moister.

A thin band of air which has lost moisture is observable in Figure 7a near the anticyclone approximately 400 km to the north of the RSP. In this location, the Eulerian derivative does not show a corresponding feature. The Eulerian derivative for the same altitude surface and time period shows an increase in local moisture in an area surrounding the Drygalski Ice Tongue. However, air parcels passing over this region did not moisten, as shown by the varied signal in the Lagrangian SAT derivative (Figure 7a). Therefore, this local moistening appears to be driven by advection toward the vicinity of the Drygalski Ice Tongue. We note that the initial level of humidity in this region was low initially allowing for increased net moisture transport

toward this region. An area with a negative Lagrangian SAT derivative exists over the edge of the RIS which is counter to our expectation based on the latent heat flux displayed in Figure 6.

The Eulerian derivative and Lagrangian SAT derivative of potential temperature at the same altitude and time period are shown in Figures 7c and 7d. The Lagrangian SAT derivative (Figure 7c) shows that air passing over the edge of the RIS and the RSP was weakly warming, while air passing over the rest of the Ross Sea was weakly cooling. Air passing over the Trans-Antarctic Mountains was dominated by cooling. Figure 7d shows the Eulerian derivative of potential temperature for this same altitude and time period. Warming was observed over the Trans-Antarctic Mountains and the northwestern coast of the Ross Sea, while a cooling trend was observed over the Ross Ice Self and the southern Ross Sea. The Lagrangian SAT derivative shows a clear warming signal within a significantly sized air mass, approximately 200 km by 100 km, located over the RSP which was providing a strong heat flux (Figure 6). Note that the size of the air mass impacted by the surface fluxes was estimated from examination of the trajectories, the changing values along these pathways, and also the resultant derivatives displayed in Figure 7.

4. Discussion

From 1800 UTC on 22 November until 1200 UTC on 23 November, AMPS predictions for wind direction performed relatively poorly (Figures 5f–5h). AMPS predicted several discontinuities in wind direction, and consecutive forecasts did not agree on wind direction. During this period, AMPS consistently predicted weak wind speeds (Figures 5a–5c). The CMET balloon observed variable wind directions and wind speeds, suggesting that this period lacked significant synoptic-scale forcing in terms of a pressure gradient because of the combination of the anticyclone and cyclone, though we note that the differences between the AMPS forecast wind speeds and the CMET observations were worse nearer the surface and better at higher altitudes. Initially, the balloon traveled northward; between 0000 and 0600 UTC on 23 November the balloon was almost stationary and then began traveling southward. During this time the observed wind direction was variable, with a strong vertical gradient in wind direction observed. A similar pattern was also observed in the wind speed. Wind direction is difficult to accurately predict when wind speeds are low as a small magnitude change in the wind vector can cause a large change in direction (Jolly et al., 2016). The balloon was also relatively close to the significant topography of Ross Island during this period, and AMPS, as well as other similar models, are known to have difficulty modeling the effects of complex terrain (Bromwich et al., 2005; Jolly et al., 2016).

Observations made by the CMET balloon often fell between the values predicted by the different AMPS forecasts. Particularly in the wind direction field, regions where consecutive AMPS forecasts disagreed often coincided with regions where AMPS had its largest anomalies from the CMET observations. This reinforces the idea that anomalies between consecutive AMPS forecasts may be used as an indicator of the accuracy of AMPS forecast in that region.

AMPS utilizes NISE SIC data as an input (Brodzik & Stewart, 2016). These data were provided at a 25 km horizontal grid resolution and have a temporal resolution of 24 hr. While this spatial resolution is significantly smaller than the spatial extent of the RSP, it is comparable to that of the McMurdo and Terra Nova Bay polynyas. In Figure 3a the minimum SIC within these polynyas is greater than 50%. However, subpixel-sized areas of open water were observed visually during field operations within Terra Nova Bay. These areas are not identified by the NISE product as they are averaged out over the coarse resolution grid. This, in addition to the low temporal resolution of the NISE data set, will limit the ability of AMPS to model the influence these regions have on the atmosphere above (Batrak & Müller, 2018). We therefore suggest that the influence of the polynya derived from AMPS should be considered to be a low estimate particularly when the biases in the AMPS low-level winds are considered.

Lagrangian SAT derivatives were calculated over a 24 hr period, which removed the diurnal cycle but caused a loss of coherent structure in the resultant field. If a small, localized heat source existed over the 24 hr period, air in regions immediately upwind and downwind of the source, regions of open water in this case, would pass over this region and also register a heat gain. In this case, the RSP acted as a source of heat for the atmosphere, causing an increase in potential temperature for trajectories that passed over the RSP, but given the averaging over the 24 hr period and the spatial averaging inherent in our analysis a larger region was likely impacted by this heat source.

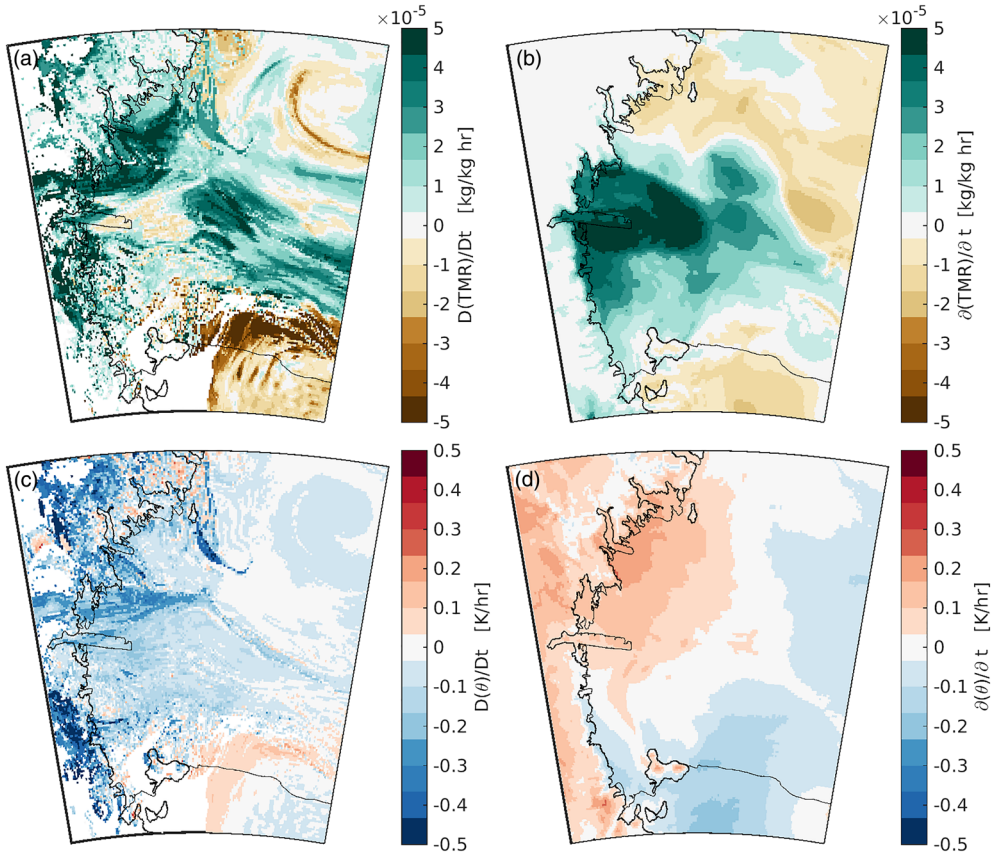

Figure 8. (a) Lagrangian SAT derivative of the total water mixing ratio over a 24 hr period starting at 0800 UTC on 23 November, calculated using trajectories launched 250 m above the surface. (b) Eulerian derivative of the total water mixing ratio at 250 m over the same 24 hr period. (c) Lagrangian SAT derivative of potential temperature over the same period. (d) Eulerian derivative of potential temperature at 250 m over the same 24 hr period.

While the end-to-end length of the trajectories varied due to spatially and temporally varying wind speeds and differences in trajectory path, lengths of approximately 1,000 km were typical (relating to a wind speed of 11.6 ms^{-1}). It can therefore be considered that very conservatively the trajectories each sampled an area of a circle with a radius of 500 km, that is, 785,000 km^2. While the RSP provided a large heat flux of ≈100 Wm^{-2} over a relatively small area of 2,500 km^2 when the effect is spread out over this wider region, this would be indistinguishable from a flux of 0.3 Wm^{-2} over the entire field. This calculation makes a minimal estimate of the impact of the RSP on the calculated Lagrangian SAT derivative field. In reality the area represented by the Lagrangian SAT derivative is likely to resemble an hourglass shape diverging upwind and downwind from the central launch point. While the heat provided by the RSP over this area would be larger than 0.3 Wm^{-2}, it would also be considerably less than 100 Wm^{-2} observed directly over the RSP. For this reason, the effect of the strong, upward heat flux from the RSP is likely difficult to discern in the Lagrangian SAT derivative field. This likely explains why Figure 7a shows air passing over the RSP becomes drier even though the polynya was providing a moisture source to the surrounding air.

In order to demonstrate the impact of a small but strong heat and moisture source such as the RSP, longer-term climatological averages likely need to be assessed. This would also remove the effect of transient events and show the long-term impact of such a heat flux. Furthermore, the impact of the RSP is expected to be stronger during the winter when the temperature derivative between the open water and the atmosphere is stronger and wind speeds are generally stronger and more consistent (Parish & Cassano, 2003).

The Lagrangian SAT and Eulerian derivatives for potential temperature (Figures 7c and 7d) generally oppose each other, particularly in areas surrounding the RSP. The Eulerian derivative indicates that air over the RSP cooled over the period of concern, while the Lagrangian SAT derivative indicated the potential temperature of air passing over the RSP increased. This highlights the importance of considering both the Lagrangian

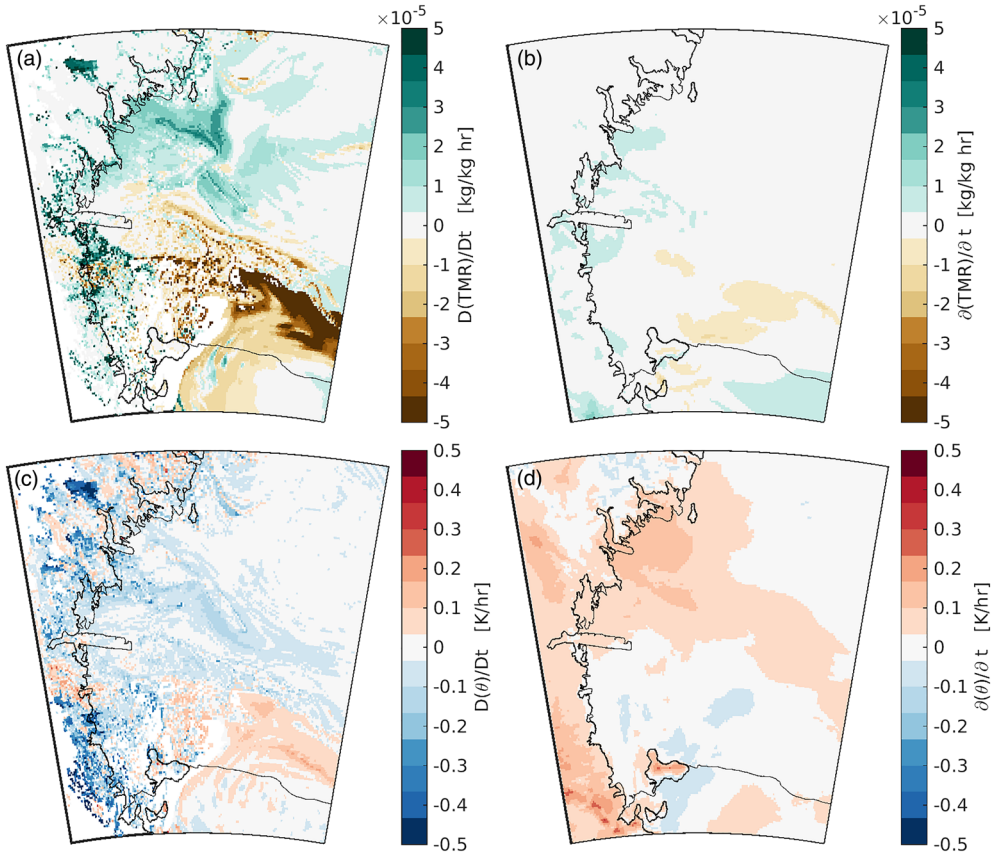

Figure 9. (a) Lagrangian SAT derivative of the total water mixing ratio over a 24 hr period starting at 0800 UTC on 23 November, calculated using trajectories launched 1,000 m above the surface. (b) Eulerian derivative of the total water mixing ratio at 1,000 m over the same 24 hr period. (c) Lagrangian SAT derivative of potential temperature over the same period. (d) Eulerian derivative of potential temperature at 1,000 m over the same 24 hr period.

SAT and Eulerian derivatives, as simple inspection of the Eulerian derivative would lead to the conclusion that the RSP did not provide a significant source of heat and caused the air above to cool. But, when the Lagrangian SAT derivative is also considered, it is found that air passing over the RSP warmed over the same period and the RSP supplied heat to the atmosphere. This likely indicates that the cooling found in the Eulerian derivative (Figure 7d) is caused by a cool body of air being advected over the RSP, replacing a warmer body of air. Thus, the RSP can be inferred to provide heat to the above atmosphere over the studied time period. We can therefore identify that the polynya in the region has a significant and near-continuous impact on the atmosphere during this period of the year.

The RSP in this period appears to have been connected to a RIS air stream event; these events occur most frequently in the austral winter (Coggins et al., 2014). Thus, we speculate that the RSP could be a significant source of local heating in the winter during and after RAS events, this being particularly significant because the temperature differential between the ocean and the overlying atmosphere will be larger in winter resulting in a larger heat flux. In addition, work detailed in Coggins and McDonald (2015) suggests that the strengthening of the Amundsen Sea Low has likely increased the frequency of RAS events over the Ross Sea region. This suggests that there may be significant trends in the atmosphere-ocean heat fluxes over the RSP, which may have in turn impacted sea ice production.

The latent heat provided by the RSP (Figure 6a) indicates potential for evaporation of water within this region, thus providing an upward moisture flux from the ocean to the atmosphere. However, this effect was not represented in Figures 7a and 7b, which show the derivatives of TWMR over the Ross Sea at 500 m. We speculate that this suggests that the evaporated moisture is not able to reach this altitude. To examine this hypothesis, we also created derivative fields at 250 and 1,000 m (Figures 8 and 9); these reveal similar results, with the 250 m showing more similarities with the 500 m result than the 1,000 m. The main difference from

the 500 m result in these cases is the larger magnitudes of change being observed at the lower, and therefore warmer and generally more moist, altitude. This potentially highlights the limited ability for moisture to mix vertically to 250 m and above in the AMPS model associated with this event. It also potentially suggests an inconsistency in the representation of humidity with the parameterization of latent heat flux (Figure 6).

5. Conclusions

This work presents meteorological observations made in situ over the Ross Sea in November using a long-duration CMET balloon. CMET observations from a single flight lasting over 70 hr are compared with forecasts made by AMPS, an operational version of the Polar WRF model used to support Antarctic operations. During this flight, the balloon made repeated soundings through the marine boundary layer and flew near both the Terra Nova and Ross Sea Polynyas.

AMPS predictions of atmospheric conditions generally compared favorably with CMET observations. Discrepancies were found to be most frequent in the wind direction, particularly during periods of weaker winds and time periods surrounding changes in wind direction. CMET observations generally fell within the range of variability found between consecutive AMPS forecasts, indicating that the forecasts bound the observations.

AMPS SIC and surface heat flux predictions indicated that the RSP was open and provided a source of heat and moisture to the atmosphere during the period of the CMET measurements. Calculation of the Lagrangian SAT and Eulerian derivatives allows the influence of the RSP on the air mass sampled by the CMET balloon to be considered. This analysis indicates that the area over the RSP provided a source of heat and that the influence of this heat source conservatively covered a region of 200 km by 100 km in this case. Evidence of diabatic heating at these levels was observed in the potential temperature derivatives. We also showed that this case was relatively representative of this time of year, and the good correspondence between AMPS and the CMET balloons suggests that our derivative calculation methodology might be more widely useful in understanding the influence of polynya on the local atmospheric environment. Given that our Lagrangian derivatives are spatial averages along trajectories integrated over 24 hr, mimicking the CMET observations, the lack of clear signs of the heat sources connected to the polynya may suggest that CMET flights must be targeted to fly almost directly over the heat sources to be most effective.

Data Availability Statement

AMPS output was retrieved from the Earth System Grid (https://www.earthsystemgrid.org/project/amps.html).

Acknowledgments
We acknowledge the National Center for Atmospheric Research and the Byrd Polar Research Center for providing AMPS output. This study was funded by a grant from the New Zealand Antarctic Research Institute (NZARI) and supported by scholarships from New Zealand Post (administered by Antarctica New Zealand) and the Department of Physical and Chemical Sciences at the University of Canterbury. We also thank Antarctica New Zealand and Programma Nazionale di Ricerche in Antartide (PNRA) for providing logistics support.

References

Alexander, S. P., Klekociuk, A. R., McDonald, A. J., & Pitts, M. C. (2013). Quantifying the role of orographic gravity waves on polar stratospheric cloud occurrence in the Antarctic and the Arctic. *Journal of Geophysical Research: Atmospheres*, *118*, 11,493–11,507. https://doi.org/10.1002/2013JD020122

Batrak, Y., & Müller, M. (2018). Atmospheric response to kilometer-scale changes in sea ice concentration within the marginal ice zone. *Geophysical Research Letters*, *45*, 6702–6709. https://doi.org/10.1029/2018GL078295

Bourassa, M. A., Gille, S. T., Bitz, C., Carlson, D., Cerovecki, I., Clayson, C. A., et al. (2013). High-latitude ocean and sea ice surface fluxes: Challenges for climate research. *Bulletin of the American Meteorological Society*, *94*(3), 403–423. https://doi.org/10.1175/BAMS-D-11-00244.1

Bracegirdle, T. J., & Kolstad, E. W. (2010). Climatology and variability of Southern Hemisphere marine cold-air outbreaks. *Tellus A Dynamic Meteorology Oceanography*, *62*(2), 202–208. https://doi.org/10.1111/j.1600-0870.2009.00431.x

Brodzik, M. J., & Stewart, J. S. (2016). *Near-real-time SSM/I-SSMIS EASE-Grid Daily Global Ice Concentration and Snow Extent, Version 5*. Boulder, Colorado USA. NASA National Snow and Ice Data Center Distributed Active Archive Center, https://nsidc.org/data/nise

Bromwich, D. H. (1989). Satellite analyses of Antarctic katabatic wind behavior. *Bulletin of the American Meteorological Society*, *70*(7), 738–749. https://doi.org/10.1175/1520-0477(1989)070<0738:SAOAKW>2.0.CO;2

Bromwich, D. H. (1991). Mesoscale cyclogenesis over the southwestern Ross Sea linked to strong katabatic winds. *Monthly Weather Review*, *119*(7), 1736–1753. https://doi.org/10.1175/1520-0493(1991)119<1736:MCOTSR>2.0.CO;2

Bromwich, D., Liu, Z., Rogers, A. N., & Van Woert, M. L. (1998). Winter atmospheric forcing of the Ross Sea Polynya, In S. S. Jacobs & R. F. Weiss (Eds.), *Ocean, ice, and atmosphere: Interactions at the Antarctic continental margin, Antarctic Research Series* (Vol. 75, pp. 101–133). https://doi.org/10.1029/AR075p0101

Bromwich, D. H., Monaghan, A. J., Manning, K. W., & Powers, J. G. (2005). Real-time forecasting for the Antarctic: An evaluation of the Antarctic mesoscale prediction system (aMPS)*. *Monthly Weather Review*, *133*(3), 579–603. https://doi.org/10.1175/MWR-2881.1

Bromwich, D. H., Otieno, F. O., Hines, K. M., Manning, K. W., & Shilo, E. (2013). Comprehensive evaluation of polar weather research and forecasting model performance in the Antarctic. *Journal of Geophysical Research: Atmospheres*, *118*, 274–292. https://doi.org/10.1029/2012JD018139

Carrasco, J. F., & Bromwich, D. H. (1993). Mesoscale cyclogenesis dynamics over the southwestern Ross Sea, Antarctica. *Journal of Geophysical Research*, *98*(D7), 12,973. https://doi.org/10.1029/92JD02821

Cassano, J. J., Nigro, M. A., & Lazzara, M. A. (2016). Characteristics of the near-surface atmosphere over the Ross Ice Shelf, Antarctica. *Journal of Geophysical Research: Atmospheres*, *121*, 3339–3362. https://doi.org/10.1002/2015JD024383

Coggins, J. H. J., & McDonald, A. J. (2015). The influence of the Amundsen Sea Low on the winds in the Ross Sea and surroundings: Insights from a synoptic climatology. *Journal of Geophysical Research: Atmospheres*, *120*, 2167–2189. https://doi.org/10.1002/2014JD022830

Coggins, J. H. J., McDonald, A. J., & Jolly, B. (2014). Synoptic climatology of the Ross Ice Shelf and Ross Sea region of Antarctica: *k*-means clustering and validation. *International Journal of Climatology*, *34*(7), 2330–2348. https://doi.org/10.1002/joc.3842

Costanza, C. A., Lazzara, M. A., Keller, L. M., & Cassano, J. J. (2016). The surface climatology of the Ross Ice Shelf Antarctica. *International Journal of Climatology*, *36*(15), 4929–4941. https://doi.org/10.1002/joc.4681

Dale, E. R., McDonald, A. J., Coggins, J. H. J., & Rack, W. (2017). Atmospheric forcing of sea ice anomalies in the Ross Sea polynya region. *Cryosphere*, *11*(1), 267–280. https://doi.org/10.5194/tc-11-267-2017

Drucker, R., Martin, S., & Kwok, R. (2011). Sea ice production and export from coastal polynyas in the Weddell and Ross Seas. *Geophysical Research Letters*, *38*, L17502. https://doi.org/10.1029/2011GL048668

Elvidge, A. D., Renfrew, I. A., King, J. C., Orr, A., Lachlan-Cope, T. A., Weeks, M., & Gray, S. L. (2015). Foehn jets over the Larsen C Ice Shelf, Antarctica. *Quarterly Journal of the Royal Meteorological Society*, *141*(688), 698–713. https://doi.org/10.1002/qj.2382

Fiedler, E. K. (2010). Ocean-atmosphere heat fluxes at the Ronne Polynya, Antarctica. *Weather*, *65*(1), 16–21. https://doi.org/10.1002/wea.436

Friedrich, L. S., McDonald, A. J., Bodeker, G. E., Cooper, K. E., Lewis, J., & Paterson, A. J. (2017). A comparison of Loon balloon observations and stratospheric reanalysis products. *Atmospheric Chemistry and Physics*, *17*(2), 855–866. https://doi.org/10.5194/acp-17-855-2017

Guo, Z., Bromwich, D. H., & Cassano, J. J. (2003). Evaluation of polar MM5 simulations of Antarctic atmospheric circulation*. *Monthly Weather Review*, *131*(2), 384–411. https://doi.org/10.1175/1520-0493(2003)131<0384:EOPMSO>2.0.CO;2

Heinemann, G. (1990). Mesoscale vortices in the Weddell Sea Region (Antarctica). *Monthly Weather Review*, *118*(3), 779–793. https://doi.org/10.1175/1520-0493(1990)118<0779:MVITWS>2.0.CO;2

Hole, L. R., Bello, A. P., Roberts, T. J., Voss, P. B., & Vihma, T. (2016). Measurements by controlled meteorological balloons in coastal areas of Antarctica. *Antarctic Science*, *28*(05), 387–394. https://doi.org/10.1017/S0954102016000213

Holland, P. R., & Kwok, R. (2012). Wind-driven trends in Antarctic sea-ice drift. *Nature Geoscience*, *5*(12), 872–875. https://doi.org/10.1038/ngeo1627

Jolly, B., McDonald, A. J., Coggins, J. H. J., Zawar-Reza, P., Cassano, J., Lazzara, M., et al. (2016). A validation of the Antarctic Mesoscale Prediction System using self-organizing maps and high-density observations from SNOWWEB. *Monthly Weather Review*, *144*(9), 3181–3200. https://doi.org/10.1175/MWR-D-15-0447.1

Nigro, M. A., Cassano, J. J., & Knuth, S. L. (2012). Evaluation of Antarctic Mesoscale Prediction System (AMPS) cyclone forecasts using infrared satellite imagery. *Antarctic Science*, *24*(02), 183–192. https://doi.org/10.1017/S0954102011000745

Nigro, M. A., Cassano, J. J., & Seefeldt, M. W. (2011). A weather-pattern-based approach to evaluate the Antarctic Mesoscale Prediction System (AMPS) forecasts: Comparison to automatic weather station observations. *Weather Forecasting*, *26*(2), 184–198. https://doi.org/10.1175/2010WAF2222444.1

Papritz, L., & Pfahl, S. (2016). Importance of latent heating in mesocyclones for the decay of cold air outbreaks: A numerical process study from the Pacific sector of the Southern Ocean. *Monthly Weather Review*, *144*(1), 315–336. https://doi.org/10.1175/MWR-D-15-0268.1

Papritz, L., Pfahl, S., Sodemann, H., & Wernli, H. (2015). A climatology of cold air outbreaks and their impact on air sea heat fluxes in the high-latitude South Pacific. *Journal of Climate*, *28*(1), 342–364. https://doi.org/10.1175/JCLI-D-14-00482.1

Parish, T. R., & Bromwich, D. H. (1997). On the forcing of seasonal changes in surface pressure over Antarctica. *Journal of Geophysical Research*, *102*(D12), 13,785–13,792. https://doi.org/10.1029/96JD02959

Parish, T. R., & Bromwich, D. H. (1998). A case study of Antarctic katabatic wind interaction with large-scale forcing*. *Monthly Weather Review*, *126*(1), 199–209. https://doi.org/10.1175/1520-0493(1998)126<0199:ACSOAK>2.0.CO;2

Parish, T. R., & Cassano, J. J. (2003). The role of katabatic winds on the Antarctic surface wind regime. *Monthly Weather Review*, *131*(2), 317–333. https://doi.org/10.1175/1520-0493(2003)131<0317:TROKWO>2.0.CO;2

Parish, T. R., Cassano, J. J., & Seefeldt, M. W. (2006). Characteristics of the Ross Ice Shelf air stream as depicted in Antarctic Mesoscale Prediction System simulations. *Journal of Geophysical Research*, *111*, D12109. https://doi.org/10.1029/2005JD006185

Petrelli, P., Bindoff, N. L., & Bergamasco, A. (2008). The sea ice dynamics of Terra Nova Bay and Ross Ice Shelf Polynyas during a spring and winter simulation. *Journal of Geophysical Research*, *113*, C09003. https://doi.org/10.1029/2006JC004048

Pezzi, L. P., de Souza, R. B., & Quadro, M. F. L. (2016). A review on the ocean-atmosphere interaction processes in regions of strong sea surface temperature gradients of the South Atlantic Ocean based on observational data. *Revista Brasileira de Meteorologia*, *31*(4), 428–453. https://doi.org/10.1590/0102-778631231420150032

Powers, J. G., Manning, K. W., Bromwich, D. H., Cassano, J. J., & Cayette, A. M. (2012). A decade of Antarctic science support through AMPS. *Bulletin of the American Meteorological Society*, *93*(11), 1699–1712. https://doi.org/10.1175/BAMS-D-11-00186.1

Roberts, T. J., Dütsch, M., Hole, L. R., & Voss, P. B. (2016). Controlled meteorological (CMET) free balloon profiling of the Arctic atmospheric boundary layer around Spitsbergen compared to ERA-Interim and Arctic System Reanalyses. *Atmospheric Chemistry and Physics*, *16*(19), 12,383–12,396. https://doi.org/10.5194/acp-16-12383-2016

Stenmark, A., Hole, L. R., Voss, P., Reuder, J., & Jonassen, M. O. (2014). The influence of Nunataks on atmospheric boundary layer convection during summer in Dronning Maud Land, Antarctica. *Journal of Geophysical Research: Atmospheres*, *119*, 6537–6548. https://doi.org/10.1002/2013JD021287

Tamura, T., Ohshima, K. I., & Nihashi, S. (2008). Mapping of sea ice production for Antarctic coastal polynyas. *Geophysical Research Letters*, *35*, L07606. https://doi.org/10.1029/2007GL032903

Turner, J., & Thomas, J. P. (1994). Summer-season mesoscale cyclones in the Bellingshausen-Weddell region of the Antarctic and links with the synoptic-scale environment. *International Journal of Climatology*, *14*(8), 871–894. https://doi.org/10.1002/joc.3370140805

Voss, P. B., Hole, L. R., Helbling, E. F., & Roberts, T. J. (2012). Continuous in-situ soundings in the Arctic boundary layer: A new atmospheric measurement technique using controlled meteorological balloons. *Journal of Intelligent & Robotic Systems*, *70*(1–4), 609–617. https://doi.org/10.1007/s10846-012-9758-6